crystals

MDPI

Article

Effect of Thermal Aging on the Reliability of Interconnected Nano-Silver Solder Joints

Yangning Tian [1,2,†], Xiaodong Jian [2,†], Mingrui Zhao [2], Jiahao Liu [2], Xuanjun Dai [1], Bin Zhou [2,*] and Xiaofeng Yang [2,*]

[1] School of Mechanical and Control Engineering, Guilin University of Technology, Guilin 541000, China; 2120211145@glut.edu.cn (Y.T.); daixuanjun@glut.edu.cn (X.D.)
[2] The Science and Technology on Reliability Physics and Application of Electronic Component Laboratory, The 5th Electronics Research Institute, Ministry of Industry and Information Technology, Guangzhou 510610, China; jianxiaodong_gdut@126.com (X.J.); 2122031509@s.xmut.edu.cn (M.Z.); liujiahao@ceprei.com (J.L.)
* Correspondence: zhoubin@ceprei.com (B.Z.); yangxiaofeng@ceprei.com (X.Y.)
† These authors contributed equally to this work and should be considered co-first authors.

Abstract: Due to the growing demand for ultra-high-density integrated circuits in the integrated circuit industry, flip-chip bonding (FCB) has become the mainstream solution for chip interconnection. In flip-chip bonding (FCB), however, alloy solder is no longer adequate to meet the high heat dissipation demands of high-power devices with over 100 kW/cm^2 in power density due to its low reflow temperature. Nano-silver solder, on the other hand, exhibits superior thermal and electrical conductivity, making it an excellent alternative to traditional solder for FCB. This study explored nano-silver's thermal reliability and electrical performance as a solder material. The following results were obtained through temperature cycle (with temperatures ranging from −55 to 150 °C) and high-temperature storage experiments (with applied temperatures of over 170 °C). The results indicate that as the duration of the high-temperature storage increased, the grain continued to coarsen, resulting in an average pore size transition from 0.004 to 0.072 μm^2. A strong correlation coefficient of 0.9913 was observed between the duration of high-temperature exposure and the porosity within the time range of 0–200 h. Following the reliability test, the shear strength of the nano-silver interconnect samples showed varying degrees of decrease. The bonding effect with the nano-silver layer can be enhanced, and the thermal reliability can be improved by depositing Ni/Ag on the surface of Cu, making it less prone to cracking. Regarding the electrical performance, the square resistance of the nano-silver interconnect structures increased by 35% after the reliability test. This indicates a significant degradation in the electrical reliability of nano-silver interconnects under temperature stress.

Keywords: nano-silver; porosity; shear force; reliability; square resistance

check for updates

Citation: Tian, Y.; Jian, X.; Zhao, M.; Liu, J.; Dai, X.; Zhou, B.; Yang, X. Effect of Thermal Aging on the Reliability of Interconnected Nano-Silver Solder Joints. *Crystals* **2023**, *13*, 1630. https://doi.org/10.3390/cryst13121630

Academic Editor: Umberto Prisco

Received: 13 October 2023
Revised: 1 November 2023
Accepted: 6 November 2023
Published: 24 November 2023

1. Introduction

Since the advent of the information age, integrated circuits have become increasingly large in scale and have rapidly improved in performance. The critical dimensions of transistors have reached the nanometer level, which poses higher demands on interconnect technology. Traditional wire bonding techniques introduce a significant parasitic resistance and capacitance and have lower thermal and mechanical reliabilities. They are no longer suitable for the current trend of smaller dimensions and higher densities in bonding [1].

A new solution for high-density interconnection is provided by flip-chip bonding technology, enabling higher-density I/O interconnects (400/cm^2 for wire bonding and 1600/cm^2 for inverted bonding) and shorter interconnect lengths (from the millimeter scale to micrometer scale). The parasitic resistance and capacitance are reduced (from 0.03 Ω and 0.006 pF to 0.002 Ω and 0.001 pF), the signal transmission efficiency and speed are enhanced, and the volume of packaging products is further reduced (overall volume reduction of 60–90%) [2,3].

However, the ultra-high interconnect density has risen in a severe thermal environment. For instance, high-power devices generally generate substantial heat with operating temperatures as high as 200 °C. For example, advanced high-power semiconductor devices such as power MOSFET and insulated gate bipolar transistors (IGBTs) generally present an ultra-high power density of over 100 kW/cm^2, which is almost over 10 times higher than conventional electronic devices [4].

In addition, according to a reliable survey, 50% of integrated circuit failures are caused by heat. For every 2 °C increase in temperature, the performance of the chip decreases by 10%. The miniaturization of all integrated circuits can be attributed to thermal management [5]. In microelectronic packaging, the solder that connects the semiconductor and the substrate serves as the pathway for circuit connection and heat dissipation. It strongly affects the heat dissipation, mechanical support, and conductivity of integrated circuits [6,7]. However, conventional flip-chip bonding (FCB) with alloy solder bumps has limitations in terms of its low reflow temperature and the formation of intermetallic compounds [8]. Consequently, the search for a welding material that retains good electrical and thermal conductivity even in high-temperature environments becomes imperative.

Nano-silver solder offers superior thermal and electrical conductivity, making it an excellent alternative to conventional solder materials [9,10]. The particle size of sintered silver solder has also evolved to include micro-silver solder paste, nano-micro hybrid solder paste, and nano-silver solder paste. As the silver particles shrink in size, the temperature and pressure requirements for the sintering process reduce accordingly. Due to the surface effects, the sintering temperature of nano-silver particles has been lowered to 200 °C, enabling low-temperature sintering. Researchers such as Wang et al. from the Harbin Institute of Technology have even achieved pressureless sintering at 150 °C [11]. Lower sintering temperatures can reduce the adverse effects of temperature on chips during the sintering interconnection process. Additionally, sintered nano-silver exhibits excellent properties similar to bulk silver, including a high melting point, high thermal conductivity, excellent electrical conductivity, and high mechanical strength. Moreover, nano-silver solder paste possesses a certain self-alignment capability due to its surface tension, which allows for the self-correction of misalignment errors within a certain range [12–14].

However, current studies on nano-silver are generally focused on the bonding mechanism of sintered nano-silver, in which the organic solvent evaporates under specific temperature and pressure conditions, resulting in the aggregation and connection of nano-silver particles to form a porous network-like structure, thus achieving the bonding of the two ends of the nano-silver layers and exhibiting certain physical properties of bulk silver [14–16]. However, due to a limited heating time, low pressure, and the presence of organic solvents and other additives, the sintered nano-silver body is not sufficiently dense after the sintering process, resulting in the formation of many small pores. Under high-temperature conditions, atoms at the surface of the grains have higher energies and weaker binding forces, leading to diffusion. The predominant form of diffusion is grain boundary diffusion, where atoms form along the grain boundaries, resulting in tighter bonding between grains. During the diffusion process, the small voids between the grains are gradually filled, and the growth and merging of grains lead to the voids between them also fusing and increasing in size. This results in a higher porosity of visible pores, and the linker that is formed in the sintered body is more compact [17–19].

There are still limitations in the current research on the reliability, thermal stability, and electrical performance stability of nano-silver as a solder material for flip-chip interconnections [20]. In particular, as the scale of the semiconductor industry continues to expand, the demand for integrated circuit devices in various harsh operating conditions is increasing. This is especially true for the development of new energy industries, such as automotive powertrain chips and aerospace chips, which require higher heat dissipation capabilities. For instance, integrated circuits in the engine compartment of automobiles need to have a higher thermal reliability to prevent failures such as interconnection structure cracking caused by high temperatures and thermal shocks [21]. Further investigation on the reliability of nano-silver as a solder is needed, particularly regarding the degree of correlation between grain coarsening and high-temperature storage time, as well as the effects of Ag/Ni plating on interfacial bonding. In order to further advance the development of nano-silver interconnection technology, this study aims to investigate the microstructural evolution and main factors influencing nano-silver interconnects after undergoing reliability experiments such as high-temperature storage and temperature cycling. Furthermore, the variation in the shear strength of the interconnects and the thermal reliability impact of Ag/Ni plating on the bonding between nano-silver solder and substrates will be analyzed. Furthermore, the electrical performance changes of the nano-silver interconnects after the reliability experiments will be explored.

2. Materials and Methods

2.1. Experimental Sample

In this work, samples were prepared with 0.3 mm and 1 mm thick Cu as the base layer for nanoscale silver interconnection. On the surface of the 1 mm thick Cu base layer, a 0.002 mm thick nickel layer was applied as an anti-oxidation layer, followed by a 0.003 mm thick silver layer as a transitional layer for interconnection with sintered silver (illustrated in Figure 1). This design aims to provide anti-oxidation protection for copper and a smooth transitional layer for interconnection with the sintered silver.

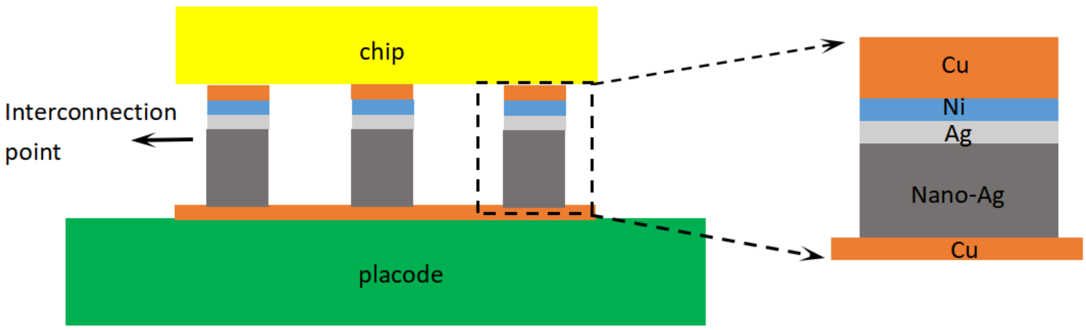

Figure 1. Schematic diagram of nano-silver solder joint interconnection.

2.2. Experimental Grouping

To explore the effects of high-temperature storage and thermal cycling on nano-silver interconnects, the experiment was divided into five groups. One group was set as the untreated control group. Two groups underwent thermal cycling experiments to investigate the occurrence of thermal mismatch and microscopic structural changes. The other two groups underwent high-temperature storage experiments for different durations to explore the effects of various high-temperature conditions on silver interconnects and the evolution of microscopic structures in high-temperature environments. Experiment groups are shown in Table 1.

Table 1. Experimental grouping.

Number	Grouping	Conditions	Strength
1	Blank group		
2	TCT	−55–150 °C	100 Circle
3	TCT	−55–150 °C	200 Circle
4	HTSL	170 °C	96 h
5	HTSL	170 °C	200 h

TCT introduction: The heating rate was 60 °C/min, low temperature, high temperature for 25 min, 20 min; each cycle was about 52 min.

HTSL: The heating rate was 21 °C/min, and furnace cooling was carried out for 1.5 h after reaching the predetermined insulation time to ensure that the sample was reduced to normal temperature.

2.3. Experimental Characterization

The following characterizations were performed on all experimental groups: The square resistance (R) of the nano-silver sintered body was measured using a four-probe testing instrument. The microscopic morphology and cross-sectional structure of nano-silver interconnects under different reliability test conditions were observed using a scanning electron microscope (SEM). Prior to sample characterization, the samples were encapsulated with epoxy resin, and then cross sections were prepared by grinding. Before SEM observation, a thin layer of gold was deposited on the sample, and conductive tape was used to drain surface charges to prevent charge accumulation in the observed area. Destructive shear force testing was conducted using a shear testing instrument (MFM1200-12121211, DRY, Yantai, China) by laterally pushing with a probe of 5 mm width at a speed of 0.5 mm/s. SEM images and sectional images were processed using ImageJ (Fiji-ImageJ2, National Institutes of Health, Bethesda, MD, USA) software to calculate the porosity of the sintered body displayed in the SEM images. The diffusion of Ni, Ag, and Cu at the bonding interface was observed using energy-dispersive X-ray spectroscopy (EDX). Ultimately, the formation effect of the nano-silver interconnects was evaluated through an observation and analysis of the microscopic morphology and cross-sectional structure. The electrical performances, mechanical properties, and reliability of the interconnect points were assessed by measuring the resistance and shear force and exploring the relationship between square resistance, shear force, and microscopic morphology.

2.4. Judgment of Data Correlation

Statistical correlation analysis enables the assessment of the relationship between different variables and helps to determine if the trends in two or more sets of data are consistent. The analysis of correlation typically involves computing correlation coefficients. The Pearson coefficient, also known as the linear correlation coefficient, is commonly utilized for linear correlation analysis and it is the most widely adopted method. The Pearson coefficient can be directly calculated in Excel to obtain the value of r between two sets of data.

The range of the correlation coefficient (r) is $[-1, 1]$.

The positive and negative relationships are determined as follows: If there is a positive correlation between two sets of data, then $r > 0$; if there is a negative correlation, then $r < 0$.

The strength of the relationship is assessed as follows:

$|r| > 0.95$: significantly correlated;

$0.8 \leq |r| < 0.95$: highly correlated;

$0.5 \leq |r| < 0.8$: moderately correlated;

$0.3 \leq |r| < 0.5$: weakly correlated;

$|r| < 0.3$: very weakly correlated.

3. Results and Discussion

3.1. Effect of the Reliability Test on the Micromorphology

The SEM characterization was performed on the experimental samples from each group to observe the overall condition of the nano-silver bonding layer. The samples were magnified to 2000× to observe the macroscopic morphology of the cross section. Subsequently, the cross-section microstructure was examined at a magnification of 9000×. The results are shown in Figure 2. The control group, which did not undergo reliability tests, exhibited a tightly bonded bonding layer without any cracking. There was no apparent boundary between the silver plating layer and the nano-silver solder layer, which indicates that the initial nano-silver solder formation is compact and well combined with the silver plating layer and the Cu surface. The initial pores with nano-scale morphology, which can be barely observed, are distributed uniformly inside the structure. With the temperature cycle and high-temperature storage treatments, the existing nano-scale pores (grains) start to merge with the adjacent ones (illustrated in Figure 3), leading to the remarkable increase in the size of sub-micro-scale or micro-scale visible pores coming along with the growing grains, which are considered as the direct influencing factors in the reliability of interconnected nano-silver solder joints.

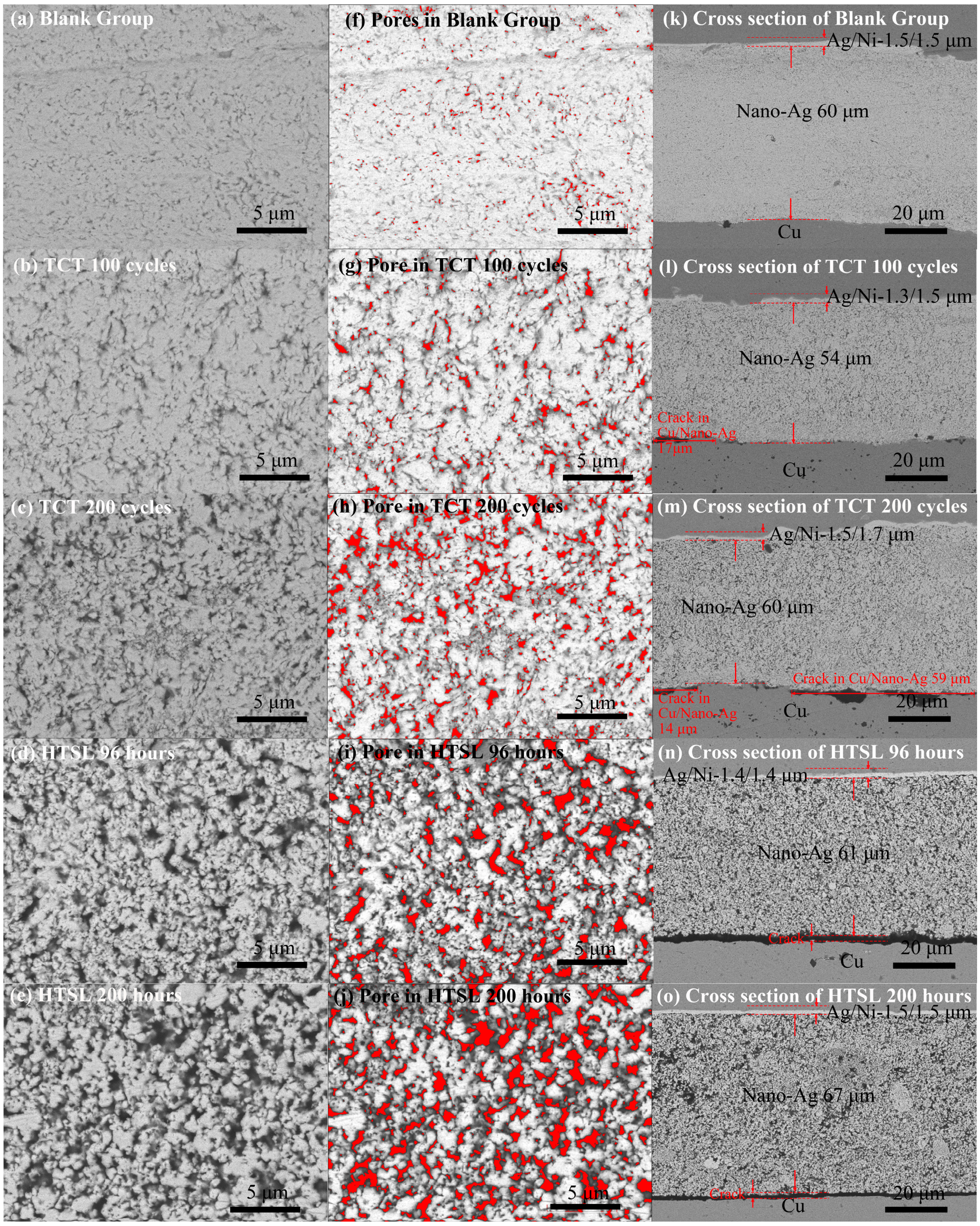

Figure 2. SEM images of experimental samples. (**a**–**e**) Microtissue images; (**f**–**j**) microtissue pore regions; (**k**–**o**) cross section images of samples.

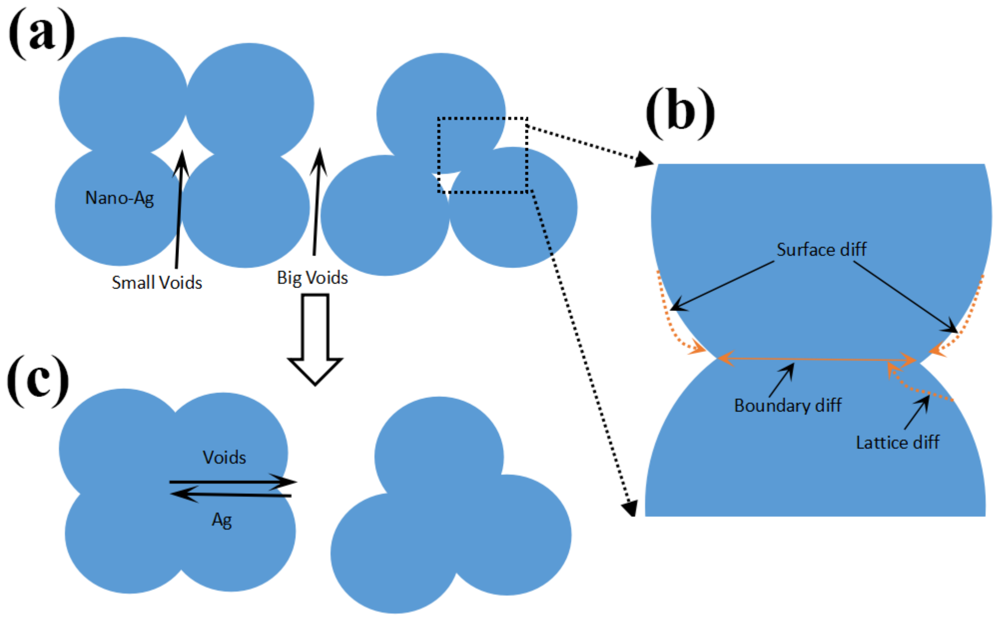

Figure 3. Schematic diagram of the evolution process of nano-silver solder sintering body in high-temperature environment. (**a**) Before coarsening; (**b**) diffusion diagram; (**c**) after coarsening.

Through a comparison with the control group sample, it can be observed from Figure 2 that the initial grain coarsening and the merging and deepening of pores begins from Group 2. The calculated porosity of visible pores is 3.1%. In Figure 2l, the crack length is observed to be 17 µm at the Cu/Nano-Ag interface. Further grain coarsening is observed in the third group, with a porosity of visible pores of 7.7%. In Figure 2m, a long crack with a length of 59 µm is observed at the Cu/Nano-Ag interface. The interface between the sintered silver and Cu exhibits further cracking [22]. In the fourth and fifth groups, compared to the control group, grain coarsening is more pronounced, and the voids significantly increase and enlarge, with calculated porosities of the visible pores of 8.3% and 13.4%, respectively, which indicates that as the high-temperature storage time increases, the grains continuously evolve towards coarsening, with continuous grain growth and aggregation of pores. Severe cracking is observed at the interface between the nano-silver solder and the Cu surface, while the interface with the silver plating layer does not show significant cracking, as shown in Figure 2n. This is because sintered silver and silver plating are the same material, which facilitates diffusion and bonding between them. The electroplated coating and substrate are more tightly connected at the atomic level, which also prevents the oxidation of the copper substrate. Therefore, the Ni/Ag plating layer can improve the bonding effectiveness between sintered silver and copper, enhancing the thermal reliability [23,24].

The porosity of visible pores, mean size, and mean number of visible pores of the SEM images were calculated using the ImageJ processing software, and the results are shown in Table 2. The ImageJ software was used to process the SEM images and calculate the porosity of the visible pores, as shown in Figure 4. The principle behind calculating the porosity of visible pores using the ImageJ software is based on the grayscale distribution curve obtained from the exposure of the image. By calculating the proportions of different grayscale levels in the image to the total area, the porosity of visible pores can be determined. From Figure 4, it can be visually observed that the porosity of visible pores and average pore size increase with the duration of high-temperature storage and the number of temperature cycles. This provides a foundation for the further exploration of the degree of correlation between the microstructure, duration of high-temperature storage, and the number of temperature cycles.

Table 2. Pore analysis results of SEM images.

Sample Number	Average Porosity %	Average Pore Size μm^2	Mean Number of Pores/400 μm^2
1	1.01	0.004	1104
2	3.12	0.013	998
3	7.74	0.034	919
4	8.30	0.041	815
5	13.4	0.072	749

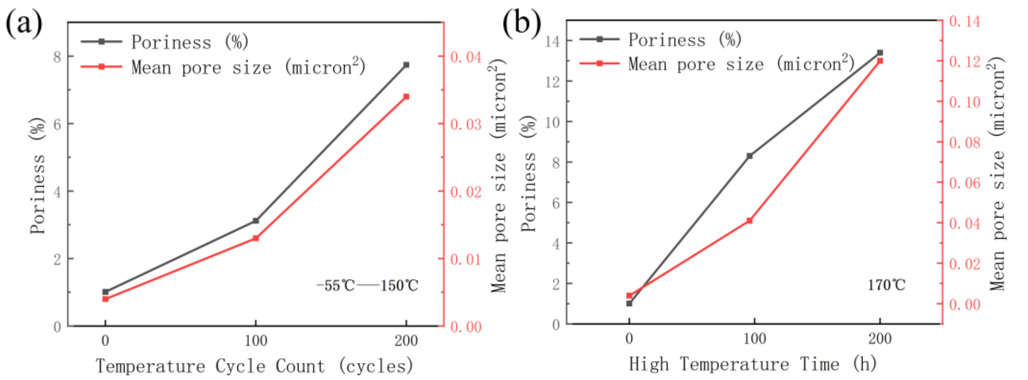

Figure 4. Porosity of visible pores and mean pore size. (**a**) Porosity of visible pores and temperature cycle times; (**b**) porosity of visible pores and high-temperature storage time of the experimental samples.

The calculation of the Pearson correlation coefficient yielded a significant positive correlation coefficient (r = 0.9913) between the duration of high-temperature storage and the porosity. This finding is consistent with previous studies in the literature, which suggest that high temperatures lead to intense molecular motion, resulting in the growth and coarsening of crystalline structures within the initially sparse sintered body. Additionally, this leads to the fusion and enlargement of small pores, consequently increasing the overall porosity of visible pores [25]. The mechanism of grain coarsening and pore fusion is shown in Figure 3; Figure 3a shows the pores before the aging test, Figure 3b is the schematic diagram of atomic diffusion, and Figure 3c is the result of grain coarsening [18].

The correlation coefficient (r = 0.9775) between the number of temperature cycles and the porosity was calculated, which is consistent with the correlation coefficient observed between the high-temperature storage times and porosity.

In addition, by extracting the high-temperature exposure time from the temperature cycling test, it was found that in 100 cycles, the high-temperature exposure time was 41.7 h, and in 200 cycles, the high-temperature exposure time was 83.4 h. By calculating the porosity and high-temperature exposure time of five sets of test samples together, a correlation coefficient (0.9811) was obtained. This result is consistent with the correlation coefficient (0.9913) obtained from only considering the high-temperature storage test. This indicates that the main influence on porosity in the temperature cycling test is the high-temperature process during the temperature cycles, while the impacts of the temperature variation process and low-temperature process on porosity are relatively small [26]. Therefore, under the same experimental time, the environment of high-temperature storage has a greater impact on the porosity than the environment of the temperature cycle.

The average pore size was calculated by dividing all of the pore areas (porosity × given area) by the pore number, and the results are shown in Figure 4.

3.2. Effect of the Reliability Tests on the Shear Strength

The shear strength of the experimental samples in each group was characterized using a push ball method. The characterization process involved pushing the samples laterally using a 5 mm wide pushing needle at a rate of 0.5 mm/s. The maximum force exerted during the entire process was recorded, and the results are shown in Figure 5. The shear strength of the group that did not undergo reliability testing was measured to be 16.9 MPa. From the characterization results, compared to the control group, the shear strength decreased by 40% in the second group, and there was a significant decrease of approximately 48% in the third group compared to the second group. The SEM images in Figure 2f–h reveal that the gap between the sintered silver and copper substrate gradually expands with the increasing duration in a high-temperature environment. This expanding gap leads to a gradual descend in strength, making it a weak point in the nano-silver interconnect. This phenomenon is attributed to the coarsening of the sintered silver grains, which results in the formation of visible pores at the sintered silver/copper interface that continuously grow and merge. Oxygen infiltrates along these voids and rapidly oxidizes the copper in the high-temperature environment, further promoting the separation of the interface [27]. Figure 2n shows that the Cu/Nano-Ag interface is through–through cracked after 96 h. This can be attributed to the presence of a larger pore size and higher porosity, which result in the deeper oxidation of copper by oxygen. Consequently, this leads to a greater degree of interface cracking.

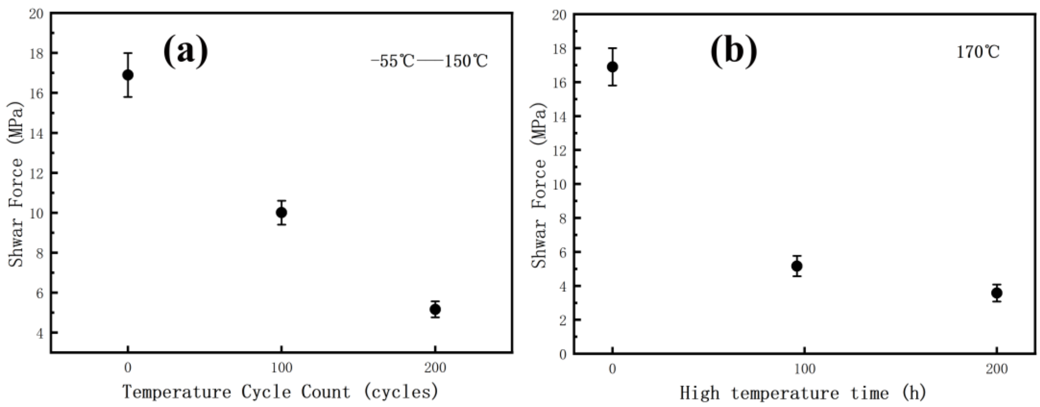

Figure 5. Shear force of experimental samples: (**a**) shear strength and temperature cycles; (**b**) shear strength and high-temperature storage time.

3.3. EDX Elemental Analysis

The elemental distributions of Ag, Ni, and Cu in the samples that were stored at a high temperature for 96 h and 200 h were characterized using an EDS analysis. The results, as shown in Figure 6, indicate that after 200 h of high-temperature storage, the Ni layer also maintains a good barrier effect, effectively preventing the oxidation of copper and maintaining a good bonding effect [28,29]. Combined with the SEM images, it can be observed that despite the significant coarsening of the sintered silver layer, the plated silver layer still maintains a good morphology. Compared to the SEM and EDS images after 96 h of high-temperature storage, it can be seen that after 200 h of high-temperature storage, a slight cracking occurs at the interface between the plated silver layer and the plated nickel layer (see Figure 6c in the red box). This suggests that the scheme of enhancing the bonding effect between nano-silver and copper by plating Ni and Ag will tend to fail after a certain period of high-temperature storage. The relevant literature has shown that the plated Ni layer tends to diffuse and merge into the copper layer after a certain period of high-temperature storage [27]. The reason for this is that the diffusion of Ni in Ag requires a higher temperature of over 427 °C [30], with a diffusion rate ranging from 10^{-14} to 10^{-12} (m^2/s) and a relatively low starting temperature of 250 °C in Cu (with a diffusion rate ranging from 10^{-13} to 10^{-11} (m^2/s)), which is attributed to the difference in the migration activation energy of Ni atoms within Cu and Ag. This also implies that a stronger bounding strength would be obtained in the Ni/Cu interface than in Ni/Ag after the high-temperature sintering process. With the volumetric contraction of nano-Ag layers caused by the high-temperature thermal treatment, which is 200 h of a long-time temperature storage in 170 °C, the tendency of interface cracking is observed between the Ni and Ag layers rather than in between Ni and Cu.

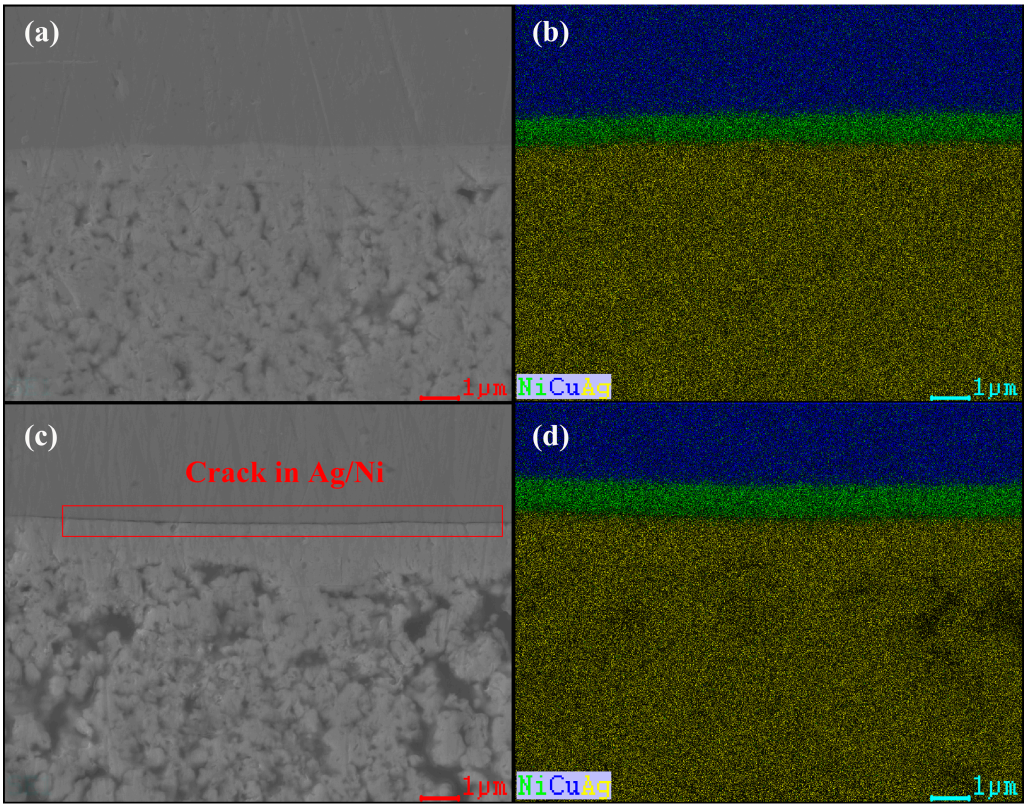

Figure 6. EDS diagram at the upper surface of sintered silver: (**a**) 96 h SEM image; (**b**) 96 h EDS image; (**c**) 200 h SEM image; (**d**) 200 h EDS image.

3.4. Analysis of the Fracture Surface Results

The cross section after the shear test is shown in Figure 7. Region A corresponds to unoxidized copper, which exhibits good bonding between the sintered silver and copper substrate. The absence of copper oxidation in this region indicates that there is no significant cracking between the copper and sintered silver in this area. In a high-temperature environment, sintered silver undergoes coarsening, leading to the formation of voids at the sintered silver/copper interface. The rapid oxidation of copper with oxygen at elevated temperatures further deteriorates the bonding effect, resulting in gradual cracking and the formation of the region indicated as D in the cross section. Using the ImageJ tool, the area percentages of each region were calculated, and they are presented in Table 3. The Pearson correlation coefficient between the area fraction of region A and shear force was found to be 0.994, indicating a strong correlation. This suggests that the copper/sintered silver interface within the entire bond layer is weaker than sintered silver/silver plating interfaces, thus determining the shear resistance capability. From the cross-sectional images Figure 7a–c, it can be observed that regions C and D increase synchronously with the increase in thermal cycling cycles. This is due to the difference in the thermal expansion capability between the sintered silver and silver plating layers caused by their microstructures, leading to crack formation. Region D experiences a greater difference in the thermal expansion capability between the sintered silver and copper due to material properties, resulting in a faster growth of the cracked and oxidized area. This leads to a decrease in the contact area and, consequently, a reduction in the bonding strength between the two layers. This reduction continues until cracking occurs. From the cross-sectional images Figure 7a,d,e, it can be observed that the area percentage of region C increases with prolonged high-temperature exposure. This is attributed to the coarsening of the sintered silver grains, which results in an increased number of voids between the sintered silver and silver plating layers. This leads to a decrease in the contact area and, consequently, a reduction in the bonding strength between the two layers, eventually leading to crack formation. Consequently, the area of the fractured interface (region C) between the sintered silver and silver plating layers increases [27].

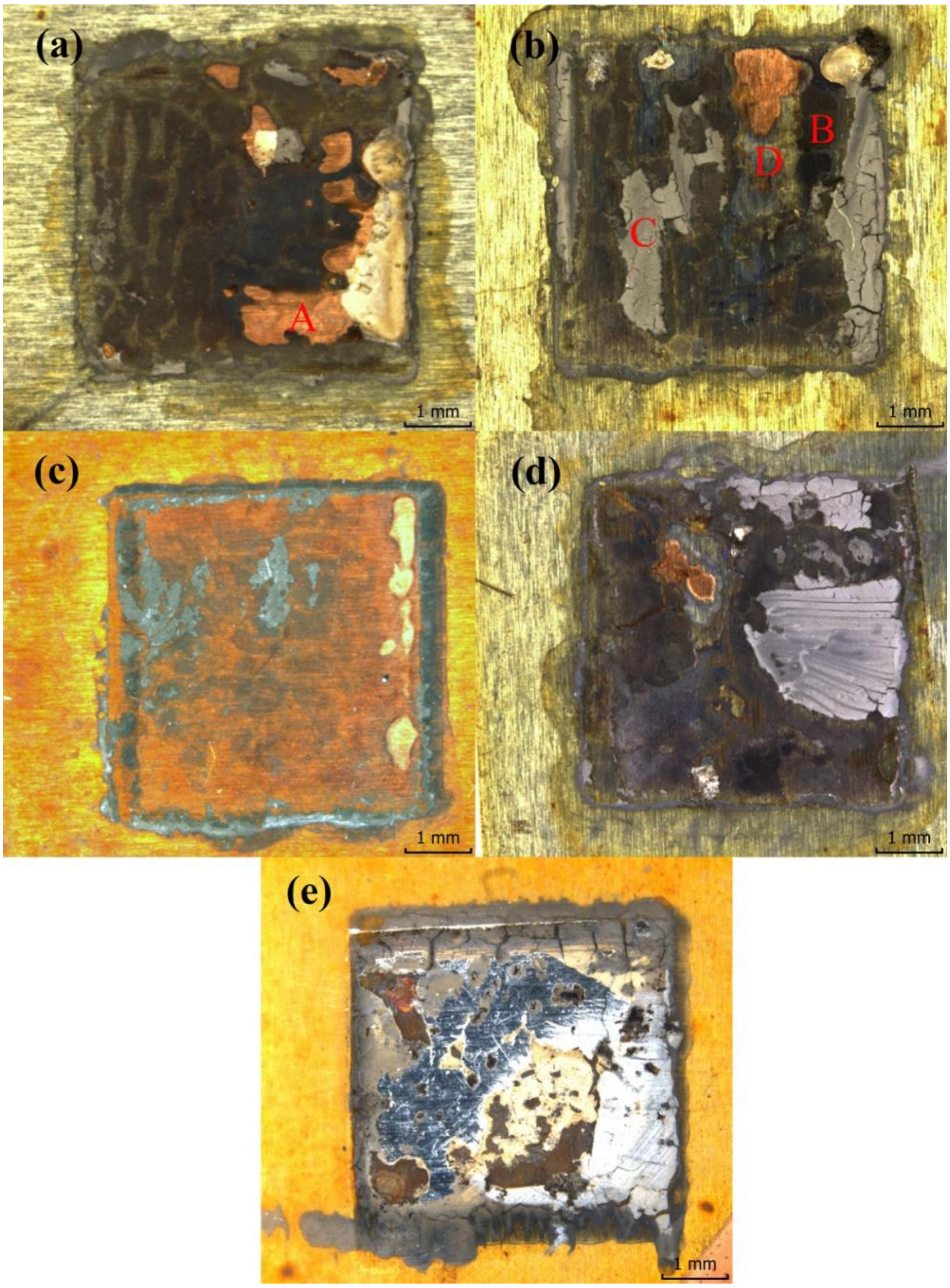

Figure 7. Sample section: A-Copper/sintered silver interface section, B-Sintered silver section, C-Sintered silver/silver-plated interface section, D-Copper/sintered silver oxidation cracking interface section; (**a**) control group; (**b**) 100 temperature cycles; (**c**) 200 temperature cycles; (**d**) high-temperature storage for 96 h; (**e**) high-temperature storage for 200 h.

Table 3. A, B, C, and D areas' area scores (as shown in Figure 7a,b).

Group Number	1	2	3	4	5
Area A area%	8.58	4.38	2.48	2.33	1.85
Area B area%	35	26	13	26	29
Area C area%	15	22	23	20	41
Area D area%	41	47	62	30	25

From Figure 8, it can be observed that with the prolonged exposure to a high temperature, the growth and merging of voids in the sintered silver develop into through-thickness cracks, which continue to grow and expand. The schematic diagram depicting the high-temperature aging crack in sintered silver is presented in Figure 9. When the bonding between the two ends of the sintered silver is good, internal fractures occur within the sintered silver, forming region B in Figure 7. Cracking at the interface between the sintered silver and copper forms region D in Figure 7. The region labeled C in Figure 7 will form when there are numerous defects at the interface between sintered silver and silver plating, and there is an area of unoxidized cracking at the interface between sintered silver and copper. The region labeled A in Figure 7 will form when there are fewer defects at the interface between sintered silver and silver plating, and there is an area of unoxidized cracking at the interface between sintered silver and copper.

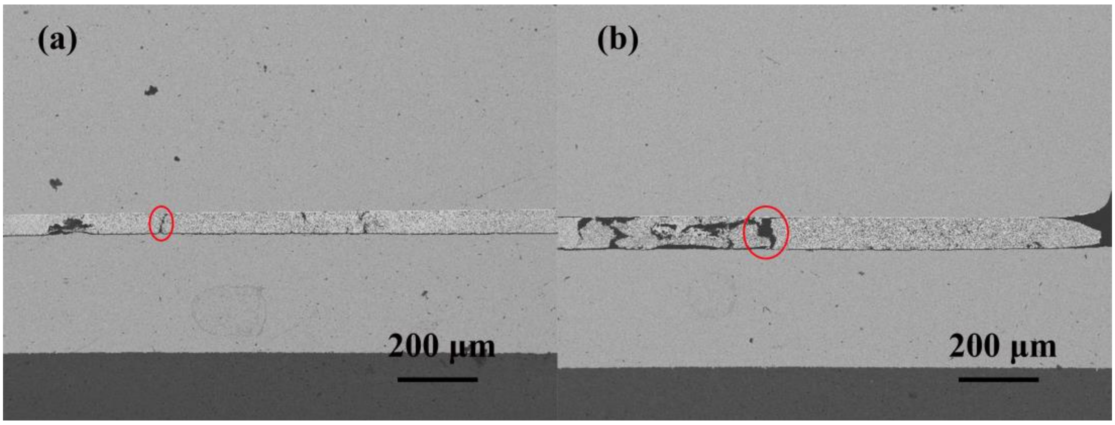

Figure 8. Red circle indicates the cracks in the sintered silver during aging. (**a**) Sintered silver interface after 96 h of high-temperature aging; (**b**) sintered silver interface after 200 h of high-temperature aging.

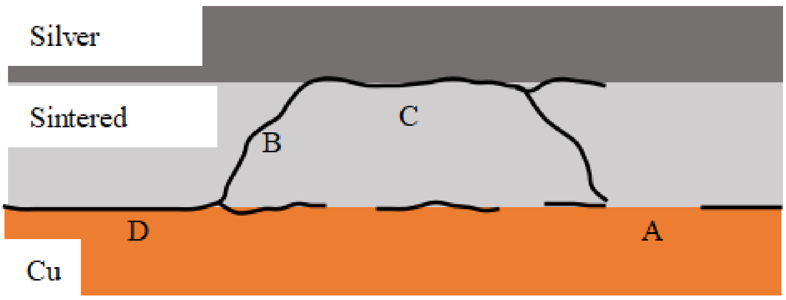

Figure 9. Schematic diagram of sintered silver cracking: A-Copper/sintered silver interface section, B-Sintered silver section, C-Sintered silver/silver-plated interface section, D-Copper/sintered silver oxidation cracking interface section.

3.5. Effect of Reliability Test on Nano-Silver Square Resistance

For each experimental sample group, the electrical properties were characterized by measuring the square resistance, as shown in Figure 10 and Table 4. The lowest resistance value in the control group was 21.3 mΩ/sq. It was reported in the literature that different sintering processes yield sheet resistance values ranging from 20 to 24 mΩ/sq [29]. This demonstrates the excellent electrical performance of the nano-silver sintered body. After 100 cycles of thermal shock, the square resistance value increased by 3.3 mΩ/sq. After 200 cycles of thermal shock, the square resistance value increased by 5.5 mΩ/sq. After 96 h of high-temperature storage, the square resistance value increased by 4.8 mΩ/sq. After 200 h of high-temperature storage, the square resistance value increased by 7.4 mΩ/sq. It can be observed that the square resistance continuously increases with an increase in the number of temperature cycles and the duration of high-temperature storage. After 200 h of high-temperature storage, an increase of 35% in the sheet resistance was observed. The Pearson's coefficient between the square resistance and the porosity of visible pores was calculated to be 0.9565, which gives a significant correlation between the square resistance and the porosity of visible pores. Generally, the value of square resistance is directly related to the density of conductive chains in the sintered body. The denser the structure of the sintered body, the more conductive chains are formed and, subsequently, the smaller the square resistance [31]. After the reliability experiments, the denser structure of the nano-Ag sintered body decreases with the increase in the high-temperature exposure time, which comes with the appearance of sub-micro-scale or micro-scale visible pores and the increase in the porosity of visible pores, resulting in the continuous decrease in the conductive paths formed inside the sintered body and the increase in the square resistance. This may even lead to the formation of crack-like defects as internal pores merge, which is even more detrimental to electrical conduction [26,32].

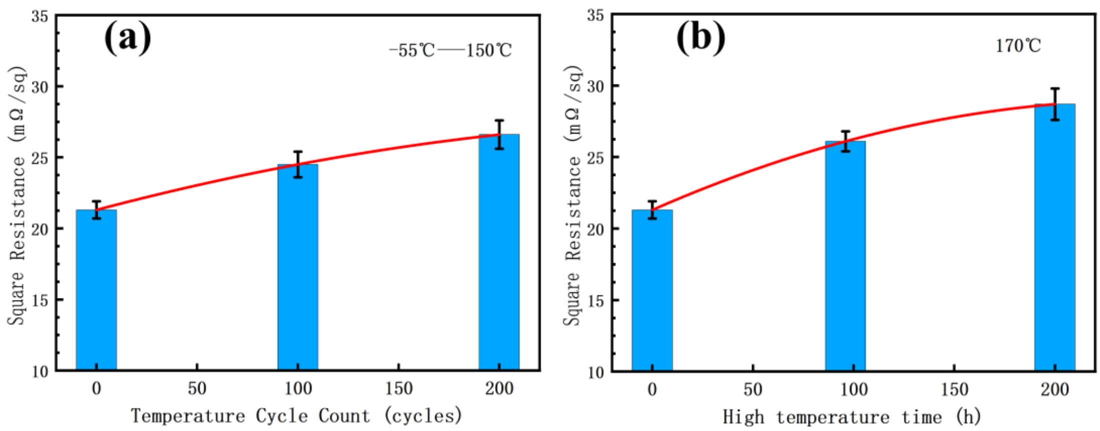

Figure 10. Square resistance of each group of test samples: (**a**) square resistance and temperature cycles; (**b**) square resistance and high-temperature storage time.

Table 4. The results of the square resistance measurement.

Group Number	1	2	3	4	5
Square Resistance (mΩ/sq)	21.3	24.6	26.8	26.1	28.7

4. Conclusions

In the present study, we investigated the microstructural properties, shear strength, square resistivity, and the impact of Ni/Ag plating layers on the reliability of nano-silver interconnect specimens under high-temperature storage and thermal cycling experiments. The degree of association between the two sets of data is evaluated using the Pearson coefficient, which is a statistical measure of correlation. Based on the analysis, the following conclusions can be drawn:

1. After high-temperature storage and thermal cycling experiments, the porosity of sintered silver continuously increases, and there is a significant positive correlation

between the time in the high-temperature storage and the porosity, with a coefficient of 0.9913. The influence of the high-temperature storage environment on the porosity of visible pores is greater than that of the temperature cycling environment under the same experimental time.
2. The bonding effect with the nano-silver layer can be enhanced, and the thermal reliability can be improved by depositing Ni/Ag on the surface of Cu, making it less prone to cracking. However, after 200 h of high-temperature storage, signs of separation between the Ni layer and Ag layer may occur.
3. After the reliability test, the shear force will experience varying degrees of decrease. This decrease can be primarily attributed to the cracking of Cu oxidation at the nano-Ag/Cu interface. The fracture surface exhibits four distinct regional forms, and the shear force shows a strong correlation with the area of close connection between the sintered silver and copper substrate, with a correlation coefficient of 0.994.
4. The electrical performances of sintered silver interconnects can be significantly impacted by reliability testing. After 200 h of high-temperature storage, an increase of 35% in the sheet resistance is observed. There is a significant positive correlation between the square resistance and the porosity of the visible pores, with a correlation coefficient of 0.9565.
5. The influence of the high-temperature storage environment on the reliability of sintered silver is greater than that of the temperature cycling environment under the same experimental time.

Author Contributions: Conceptualization, Y.T., X.J. and B.Z.; methodology, Y.T., X.D., X.J. and B.Z.; software, Y.T.; validation, Y.T., X.J. and X.Y.; formal analysis, Y.T., X.J. and M.Z.; investigation, Y.T., X.J., X.Y., X.D. and B.Z.; resources, J.L.; data curation, Y.T., X.J. and M.Z.; writing—original draft preparation, Y.T., X.J. and X.Y.; writing—review and editing, Y.T., X.J. and B.Z.; visualization, Y.T., M.Z. and B.Z.; supervision, X.D. and B.Z.; project administration, X.J., X.Y. and B.Z.; funding acquisition, X.J., B.Z. and X.Y. All authors have read and agreed to the published version of the manuscript.

Funding: This research was funded by the Guangzhou Science and Technology Project Fund, grant number 202202011247.

Data Availability Statement: The data presented in this study are available in the article.

Conflicts of Interest: The authors declare no conflict of interest.

References

1. Bindra, A. Innovative Packages Maximize MOSFETs' Thermal Performance. *Electron. Des.* **1999**, *47*, 52–64.
2. Tummala, R. Next Generation of Packaging beyond BGA, MCM and Flipchip. In Proceedings of the IMC, Plovdiv, Bulgaria, 31 July–5 August 1996.
3. Wan, J. *Research on Filling Flow in Flip Chip Packages*; Science Press: Beijing, China, 2008.
4. Wayne, R.; Johnson, J.E.L. The changing automotive environment: High-temperature electronics. *IEEE Trans. Electron. Packag. Manuf.* **2004**, *27*, 164–176.
5. Yeh, L. Review of heat transfer technologies in electronic equipment. *J. Electron. Packag.* **1995**, *117*, 333–339. [CrossRef]
6. Jiang, C.; Fan, J.; Qian, C.; Zhang, H.; Fan, X.; Guo, W.; Zhang, G. Effects of voids on mechanical and thermal properties of the die attach solder layer used in high-power LED chip-scale packages. *IEEE Trans. Compon. Packag. Manuf. Technol.* **2018**, *8*, 1254–1262. [CrossRef]
7. Feng, H.; Huang, J.; Chen, S.; Zhao, X. The new generation of power chip high temperature resistant packaging connection of domestic and foreign development review. *Weld. J.* **2016**, *37*, 120–129.
8. Kim, H.K.; Liou, H.K.; Tu, K.N. Three-dimensional morphology of a very rough interface formed in the soldering reaction between eutectic SnPb and Cu. *Appl. Phys. Lett.* **1995**, *66*, 2337–2339. [CrossRef]
9. Gomatam, R.R.; Sancaktar, E. Fatigue and failure behavior of silver-filled electronically conductive adhesive joints subjected to elevated temperatures. *Adhes. Sci. Technol.* **2004**, *18*, 849–881. [CrossRef]
10. Zeng, K.; Tu, K.N. Six cases of reliability study of Pb-free solder joints in electronic packaging technology. *Mater. Sci. Eng.* **2002**, *38*, 55–105. [CrossRef]
11. Wang, S.; Li, M.; Ji, H.; Wang, C. Rapid pressureless low-temperature sintering of Ag nanoparticles for high-power density electronic packaging. *Scr. Mater.* **2013**, *69*, 789–792. [CrossRef]
12. Siow, K.S. Mechanical properties of nano-silver joints as die attach materials. *J. Alloys Compd.* **2012**, *514*, 6–19. [CrossRef]

13. Goldmann, L. Self-alignment capability of controlled collapse chip joining. In Proceedings of the 22nd Electronic Component Conference, Orlando, FL, USA, 1 January 1972; pp. 332–335.
14. Ren, H.; Zhang, H.Q.; Wang, W.G.; Jia, Q.; Peng, P.; Zou, G.S. Research progress of Low-temperature sintering of nano-metal particle solder paste and its joint reliability. *Chin. J. Lasers* **2021**, *48*, 126–140.
15. Zhao, K.; Zhao, J.; Dai, B.; Zhang, X.; Guo, H.; Sun, H.; Zhu, J. Low temperature sintered silver connecting technology of thermal conductive diamond with large size chip. *Res. Prog. Solid State Electron.* **2021**, *41*, 65–68.
16. Zhao, L.; Jing, X.; Li, F.; Li, H.; Li, Y. Research on Reliability of Solder Joints of Nano-Silver Paste. In Proceedings of the Science and Technology Committee of China Academy of Aerospace Electronics Technology, Beijing, China, 15 December 2020; pp. 641–645.
17. Chou, T.-C.; Huang, S.-Y.; Chen, P.-J.; Hu, H.-W.; Liu, D.; Chang, C.-W.; Ni, T.-H.; Chen, C.-J.; Lin, Y.-M.; Chang, T.-C. Electrical and reliability investigation of Cu-to-Cu bonding with silver passivation layer in 3-D integration. IEEE Transactions on Components. *Packag. Manuf. Technol.* **2020**, *11*, 36–42. [CrossRef]
18. Yang, F. Study on Interconnect Behavior and Reliability of Low Temperature Sintered Nano Silver Solder Joints. Ph.D. Thesis, Harbin Institute of Technology, Harbin, China, 2021.
19. Zabihzadeh, S.; Van Petegem, S.; Duarte, L.I.; Mokso, R.; Cervellino, A.; Van Swygenhoven, H. Deformation behavior of sintered nanocrystalline silver layers. *Acta Mater.* **2015**, *97*, 116–123. [CrossRef]
20. Yan, H.; Liang, P.; Mei, Y.; Feng, Z. Progress and thinking of non-pressure low temperature sintered nano silver packaging Power electronic devices. *Chin. J. Power Sources* **2020**, *18*, 15–23.
21. Yuan, L. *Study on Microstructure and Property of Nano-Silver Paste Joint of Power IGBT and DBC by Low-Temperature Sintering*; Tianjin University China: Tianjin, China, 2015.
22. Paknejad, S.A.; Mannan, S.H. Review of silver nanoparticle based die attach materials for high power/temperature applications. *Microelectron. Reliab.* **2017**, *70*, 1–11. [CrossRef]
23. Morisada, Y.; Nagaoka, T.; Fukusumi, M.; Kashiwagi, Y.; Yamamoto, M.; Nakamoto, M. A low-temperature bonding process using mixed Cu–Ag nanoparticles. *J. Electron. Mater.* **2010**, *39*, 1283–1288. [CrossRef]
24. Hsiao, C.-H.; Kung, W.-T.; Song, J.-M.; Chang, J.-Y.; Chang, T.-C. Development of Cu-Ag pastes for high temperature sustainable bonding. *Mater. Sci. Eng. A* **2017**, *684*, 500–509. [CrossRef]
25. Tan, Y.; Li, X.; Chen, G.; Gao, Q.; Lu, G.-Q.; Chen, X. Effects of thermal aging on long-term reliability and failure modes of nano-silver sintered lap-shear joint. *Int. J. Adhes. Adhes.* **2020**, *97*, 102488. [CrossRef]
26. Wenzhi, Y.; Xiaoyun, Z.; Shuai, P. Effect of Sintering Temperature Rise Rate on Microstructure and Properties of thick copper Film. *Heat Treat. Met.* **2017**, *42*, 43–48.
27. Chen, C.; Suganuma, K.; Iwashige, T.; Sugiura, K.; Tsuruta, K. High-temperature reliability of sintered microporous Ag on electroplated Ag, Au, and sputtered Ag metallization substrates. *J. Mater. Sci. Mater. Electron.* **2018**, *29*, 1785–1797. [CrossRef]
28. Yu, F.; Cui, J.; Zhou, Z.; Fang, K.; Johnson, R.W.; Hamilton, M.C. Reliability of Ag sintering for power semiconductor die attach in high-temperature applications. *IEEE Trans. Power Electron.* **2016**, *32*, 7083–7095. [CrossRef]
29. Pešina, Z.; Vykoukal, V.; Palcut, M.; Sopoušek, J. Shear strength of copper joints prepared by low temperature sintering of silver nanoparticles. *Electron. Mater. Lett.* **2014**, *10*, 293–298. [CrossRef]
30. Tanović, N.; Tanović, L.; Fine, J. Some experimental facts about temperature-induced surface diffusion of Ag during Auger sputter depth profiling of multilayered Ni/Ag thin films. *Vacuum* **1992**, *43*, 1177–1180. [CrossRef]
31. Zhang, X.; Zhu, Y.; Wang, H. Study on effect of sintering temperature on thick film resistance. *Electron. Devices* **2012**, *35*, 394–398.
32. Gan, W.; Yue, Y.; Luo, L.; Pan, Q.; Xiong, Z. Study on preparation and sintering process of lead-free conductive silver paste. *Coat. Ind.* **2019**, *44*, 31–36.